

Classification of boiling regimes, fluids, and heating surfaces through Deep Learning algorithms and image analysis

Concepción Paz*, Adrián Cabarcos, Miguel Concheiro, Marcos Conde-Fontenla

CINTECX, Universidade de Vigo, 36310 Vigo, España

*Corresponding author. E-mail address: cpaz@uvigo.gal

Abstract

Accurate monitoring and prediction of boiling phenomena is crucial for reliable operations near critical conditions in thermal systems. In this regard, this study focuses on applying Convolutional Neural Network (CNN) algorithms for image classification to identify boiling regimes. Specifically, images used for training the Deep Learning models were acquired based on a Flow-Boiling experimental setup with Joule effect heating. Four distinct CNN architectures were employed to classify boiling phenomena under different operating conditions, covering single-phase flow, nucleate boiling, and pre-critical heat flux states. The study also examines the robustness of the models in classifying images according to the working fluid and the heating plate (non-textured and micro-textured). The performance of each CNN was evaluated using precision, recall, and F-score metrics and compared to a previously reported methodology involving downsampling, Principal Component Analysis, and a Support Vector Machine. The findings highlight the effectiveness of CNN algorithms in accurately classifying boiling regimes from images, outperforming the previous methodology. Notably, InceptionNet achieved an F-score of around 98% for plate type classification. AlexNet showed the best performance for both boiling regime and fluid type classification, with F-scores over 95%. In contrast, the previous methodology achieved a maximum F-score of around 88% for these classifications.

Keywords: Flow Boiling, Convolutional neural network, CHF, Deep Learning, Computer Vision.

Nomenclature

α, β	Learning rate and decay factor
C	Penalty term
\mathcal{L}	Cost function
m	Momentum
$\phi(x)$	Mapping function
ξ	Slack variable
w	Vector of weight coefficients
T_{wall}	Wall temperature

Acronyms

CHF	Critical Heat Flux
CNN	Convolutional Neural Networks
DL	Deep Learning
SVM	Support Vector Machine
ONB	Onset of Nucleate Boiling

1. Introduction

Boiling, and particularly nucleate boiling, is a complex and highly efficient process for heat transfer [1]. Specifically, this phenomena is commonly depicted through curves correlating heat flux to wall temperature, where the onset of nucleate boiling (ONB) within these curves depicts the initiation of vapour bubble formation [2], [3]. This nucleate boiling region, starting with ONB and characterized by its high thermal efficiency, is widely applied across numerous industries and processes, including renewable energy, air conditioning, nuclear power reactors, and electronics [4], [5]. However, a critical limit known as the critical heat flux (CHF) imposes a restriction on the amount of heat that can be dissipated from a surface during nucleate boiling [6]. Exceeding this limit causes vapour bubbles to merge, forming an insulating layer on the surface, hindering heat transfer and resulting in a rapid rise in wall temperature, leading to transition and film boiling regimes [7], [8]. This situation, commonly termed as boiling crisis, poses risks for thermomechanical devices, making it imperative to avoid exceeding the CHF limit for safe operation [9].

In this regard, despite decades of research and practical application, boiling remains a complex phenomenon, with mass and energy transfer mechanisms that are not yet fully understood [10], [11]. Consequently, despite significant advances in the development of techniques aimed at delaying boiling crises (e.g., by employing nanofluids and micro-structures machined through modern fabrication technologies [12]), most thermal systems operate with significant safety margins due to these persistent uncertainties, particularly near the CHF [13]. In fact, recent research highlights the importance of developing strategies for enabling accurate real-time monitoring and measurement of boiling regimes to promote reliable operations in near-CHF conditions, thereby minimizing the risk of thermal runaway-induced accidents [14].

In this sense, several experimental approaches have been proposed to accurately predict and classify boiling regimes. These traditional methods are usually based on thermocouples or electrical resistance-based detection techniques to identify boiling crises [15], [16]. However, these wire-based attachments usually have the disadvantage of substantially increasing the costs of boiling devices, and being intrusive methods that are noise-sensitive approaches that can disturb the fluid flow.

On a different note, pioneering research by Ponter and Haigh [17] explored the use of acoustic emissions from bubbles, suggesting that the presence of boiling is accompanied by audible sounds. Changes in these boiling sounds, observed along the boiling curve, can be noted, and acoustic emissions can therefore be utilized for boiling regime classification purposes. Recently, Sinha et al. [18] employed this method to conduct in-situ detection of CHF using acoustic signals and provided feedback control during boiling crisis. Their approach involved analysing the frequency spectrum of audible sound during various boiling stages and detecting a shift in peak frequency at CHF. However, it should be noted that in real industrial settings, it remains a significant challenge for acoustic analysis to distinguish target acoustic signals from high-level background noise [19].

Additionally, non-intrusive studies based on the use of high-speed cameras have also been capable of detecting significant differences between natural convection, pool boiling, transition boiling, and film boiling regimes [20]. Boiling images have garnered significant attention because frames captured through experimental setups provide detailed and valuable insights into bubble dynamics, which can be related to the regimen and being a cost-effective and portable method. Recent research by Al-Hindawi et al. [21] highlights the fundamental importance of detecting CHF and understanding the primary mechanisms contributing to its development through image analysis. Nonetheless, the utilization of such data often entails drawbacks, chiefly associated with time-consuming processes. In this sense, recent advances in Deep Learning (DL) can be useful for image processing and automatic data extraction in boiling applications. For instance, Hobold and da Silva [20] proposed a Machine Learning methodology achieving over 93% accuracy in identifying pool boiling regimes by applying Principal Component Analysis (PCA) for dimensionality reduction followed by supervised learning algorithms, including Support Vector Machine (SVM) and Neural Networks. A similar approach was later employed for heat flux quantification in nucleate boiling frames [22]. However, it should be noted that these previous

studies applied a dimension reduction approach for subsequent application of Machine Learning, whereas in recent years, Convolutional Neural Networks (CNNs) have emerged as a type of DL algorithm specifically designed for image processing and recognition tasks. Compared to those Machine Learning models, CNNs require less pre-processing as they can automatically learn feature representations from raw input images [23]. Indeed, recent research has demonstrated the promising application of CNNs for tasks such as heat flux prediction and tracking local bubble behavior, including bubble generation, coalescence, collision, merging, and rupture events [24], [25]. Additionally, CNNs have proven effective in distinguishing between condensing flow pattern images of methane and tetrafluoromethane in horizontal circular tubes, achieving an accuracy exceeding 90% [26].

However, according to Rashidi et al. [27], the use of Machine Learning and, by extension, CNN algorithms, for classifying boiling regimes is still relatively new. Moreover, previous studies in this area have often present and compared a small number of algorithms [24], [28], emphasizing the need for a thorough comparison between different methods. This is especially important because the effectiveness of CNN algorithms can vary greatly depending on the specific task and the type of information available [29]. Thus, in this specific study, four CNN architectures – AlexNet, ResNet, InceptionNet and a basic network used as reference – were employed and compared to predict the boiling regime (single-phase, nucleate boiling, and CHF) using images captured in a flow-boiling experimental setup, where boiling is induced by Joule heating of a steel plate. The algorithms were also used to classify the working fluid shown in those images (water, water-ethylene glycol mixture, and hydrofluoroether), as well as to identify the type of plate surface (micro-textured or non-textured). Model performance was evaluated using precision, recall, and F1-score metrics. CNN Algorithms were also compared with a previous methodology reported by the literature [20].

2. Experimental setup and methodology

The data utilized for training and testing the Deep Learning algorithms was obtained using the experimental setup illustrated in Figure 1.a. This setup, extensively described in prior research [7], [30], [31], consists of two main parts: a study section outlined by a blue dashed line in Figure 1.a, and supplementary subsystems facilitating the adjustment and measurement of main variables such as bulk temperature, pressure, or the volumetric flow rate. Specifically, the study section employed in this work comprises a rectangular channel measuring 10 x 25 x 320 mm with adjustable inclination. Additionally, for this specific research, heat flux on this wall was generated through Joule heating of a 1 mm thin stainless steel plate using an electric power source. A more in-depth examination of this heating method can be found in reference [32], while the associated uncertainties related to this particular flow boiling setup are discussed in reference [7].

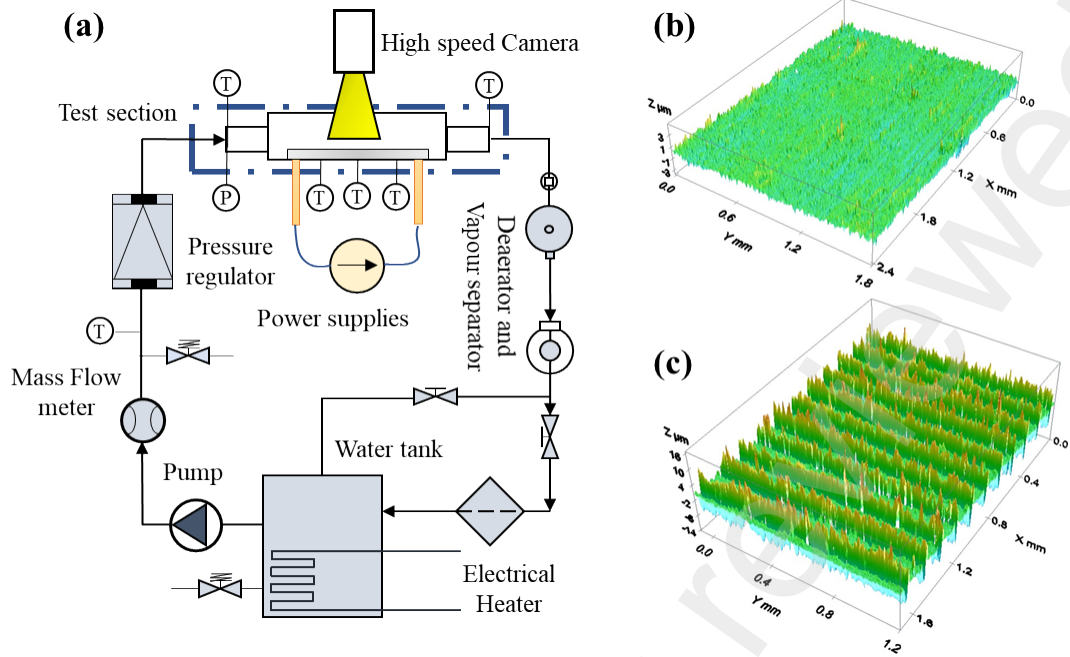


Figure 1. (a) Schematic of the flow boiling experimental setup. **(b)** Profile of a non-textured surface. **(c)** Profile of a transversal direction micro-textured surface.

Furthermore, it is important to note that two types of heating plates were specifically utilized in this study. The first type involves a reference plate, which was assessed using an optical surface profiler PLu Neox Sensofar (as shown in the measurement depicted in Figure 1.b). The profiler was configured for confocal microscopy operation mode, resulting in roughness parameters equal to $R_a = 314 \text{ nm}$ and $R_q = 406 \text{ nm}$. On the other hand, the second type incorporates a microtextured surface modification of a reference plate, prepared using a Yb:KYW (Ytterbium doped Potassium Itrium Tungstate) laser source with a wavelength of 520 nm. Specifically, an irradiance of $2.1 \times 10^{12} \text{ W/cm}^2$ was applied for this process. Figure 1.c presents a measurement of this microtextured surface, yielding roughness parameters equal to $R_a = 1.68 \mu\text{m}$ and $R_q = 2.81 \mu\text{m}$. It is also important to note that, within this plate type group, micro-textures in both longitudinal and transverse directions were considered for this work.

Regarding the experimental methodology, once specific operating conditions were defined, the procedure followed the approach detailed in prior work [7]. Specifically, tests were conducted with variations in inlet velocities (0.2 to 0.8 m/s), inlet temperatures (20 to 95°C), pressures (130 to 220 kPa), and channel inclinations (0°, 180°, 225°, and 270°). Three different working fluids were used: distilled water, a 50% ethylene glycol (EG)-water mixture, and hydrofluoroether. Both the reference plate and micro-textured heating plate were also considered in these experiments.

The procedure involved incrementally increasing the power applied to the heating plate by adjusting the electrical current in increments of 0.5 A. A high-speed camera captured frames at intervals of every 0.1 MW/cm². Frames captured before the onset of nucleate boiling were categorized as "Non-Boiling", those after ONB in the nucleate boiling region as "Boiling", and the last record of images taken, if the critical heat flux for that specific test was attained, was designated as "Pre-CHF". As a result, a database comprising 3800 images was utilised to train Deep Learning models. Additionally, an illustrative collection of images taken from this specific flow boiling setup, categorised into each of these groups, can be found in [Appendix A](#).

3. Deep learning models

Drawing from the experimental setup and methodology outlined in section 2, a database of images captured at different points along the boiling curve was obtained. This dataset includes observations conducted with three distinct fluids and two types of plates (non-textured and micro-textured). Utilizing this dataset, Deep Learning algorithms, and particularly CNN models, can autonomously discern patterns within the images and classify new frames based on their training stage. Specifically, this study presents a comparative analysis considering four distinct architectures (ResNet, InceptionNet, AlexNet, and a basic CNN architecture used as a reference), which are described below.

3.1. Overview of CNN architectures

Convolutional Neural Networks are classified as feed-forward networks that conduct spatial mapping on existing data [33]. This process transforms the data into a new space, facilitating the identification of relevant features. Additionally, CNN models are composed of three primary types of layers: convolutional layers, pooling layers, and fully connected layers. Each of these layers is briefly outlined below [34], [35]:

- **Convolutional layer.** This layer enables the extraction of relevant image characteristics by employing convolutional filters. During this process, the input image undergoes convolution with N filters, resulting in N feature maps, each emphasizing unique features. The convolution operation involves sliding filters horizontally and vertically across the input image. Subsequently, a non-linear activation function is applied to the resulting maps to compute the final output feature map.
- **Pooling layer.** Within these layers, essential features extracted from convolutional layers are stored, and by downsampling, the spatial resolution of the feature maps is reduced. This process ensures that CNNs can effectively process input matrices with a large number of elements, such as images. Two primary types of pooling layers are typically employed: max pooling and average pooling. Max pooling selects the maximum value within each patch of the feature map, while average pooling calculates the average value within each patch [34].
- **Fully connected layer.** This layer functions similarly to the conventional fully connected networks in traditional machine learning models. It receives the output generated from the initial layers of CNN, where convolution and pooling operations are repeatedly applied. Following this, the output is transmitted to the fully connected layer, where the ultimate output is determined by computing the dot product between the weight vector and the input vector.

Based on the proper combination of these previous layers, numerous architectures have been proposed over time [36]. A description of each of the architectures considered in this work is provided below:

- **Basic CNN.** This term refers to one of the most fundamental CNN architectures for image processing, comprising only two convolutional and pooling layers [37], [38], as illustrated in Figure 2. This network serves as a reference model for comparing the performance of more advanced models (specifically AlexNet, ResNet, and InceptionNet, also described below). For this specific study, the technical details of each layer in Figure 2 are presented in detail in Appendix B.
- **AlexNet.** This architecture consists of five convolutional layers and three fully connected layers, as depicted in Figure 2. Notably, it was one of the pioneering deep convolutional neural networks to replace the traditional sigmoid activation function following the convolution layers with rectified linear units, resulting in improved performance compared to earlier networks. Additionally, after the last max-pooling layer, the output is flattened into a

vector and then forwarded to the first fully connected layer [36]. In the original architecture, the final fully connected layer comprises 1000 neurons, aligning with the number of classes in the dataset for which the network was initially trained. However, in this specific work, the number of final connections was adjusted based on the number of classes to the study. Details of each of the layers depicted in Figure 2 are presented in Appendix B.

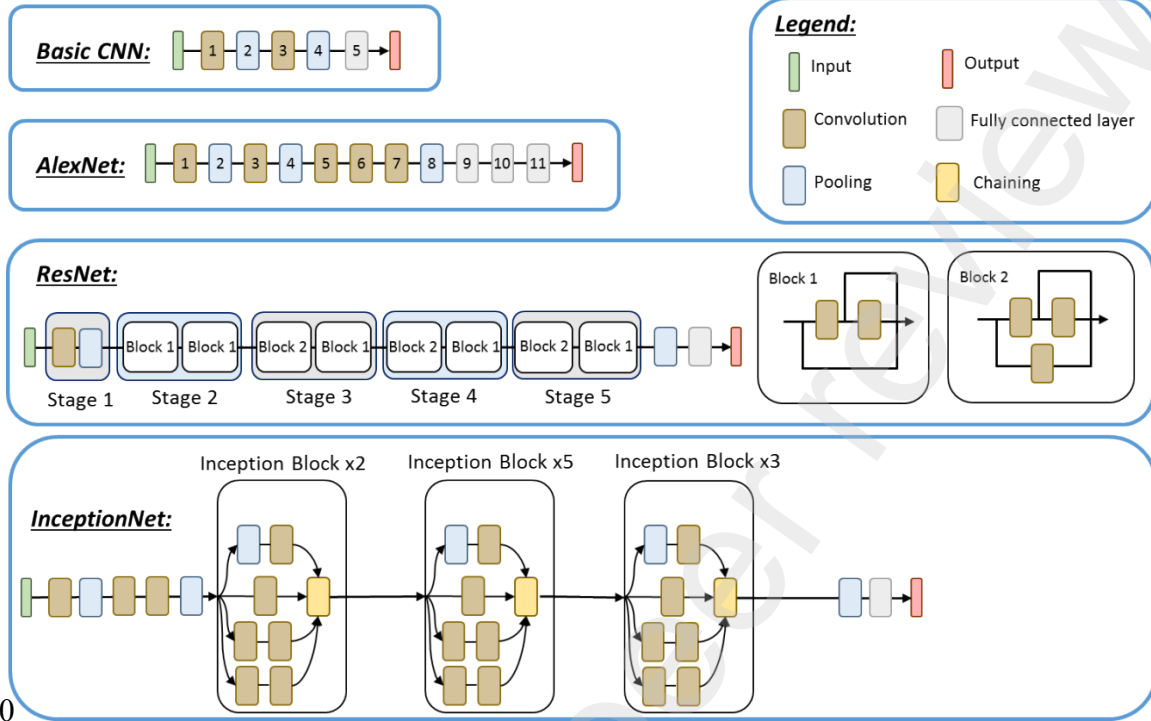


Figure 2. Schematic about CNN architectures considered in this work [35–37], [40], [41].

- **Residual Network (ResNet).** This architecture seeks to boost the efficiency of network training by introducing shortcut connections, also referred as identity connections [39]. These connections enable information to skip one or more layers, which helps overcome the issue of vanishing gradients often seen in deep networks. By utilizing activations from earlier layers, these shortcuts accelerate learning and prevent performance degradation. Technical details of each of the stages shown in Figure 2 can be found in Appendix B.
- **InceptionNet.** As it can be seen in Figure 2, this architecture stands out for its utilization of multiple parallel convolutional layers with diverse filter sizes, enabling the network to capture features across various scales and resolutions simultaneously. In contrast to CNN architectures like AlexNet, which usually employ single filter sizes per layer, Inception employs a combination of filters with different sizes concurrently. This is achieved by simultaneously applying 1×1 , 3×3 , and 5×5 convolutions, alongside pooling operations [36]. Subsequently, the outputs generated from these operations are concatenated and passed on to the next layer. An in deeper overview of the inception blocks shown in Figure 2 can be found in reference [40].

3.2. Implementation and performance assessment

The architectures detailed in section 3.1 were trained using Matlab 2023 and the Deep Learning Toolbox. Particularly, as a pre-processing step for each architecture, images were rescaled and transformed according to the considerations depicted in Table 1.

Table 1. Preprocessing required for input images according the algorithm selected

<i>Algorithm</i>	<i>Pre-processing</i>
AlexNet	Input images resized to 227 x 227 pixels. 3-channel images in RGB scale
ResNet	Input images resized to 224 x 224 pixels. 3-channel images in RGB scale
InceptionNet	Input images resized to 224 x 224 pixels. 3-channel images in RGB scale
CNN reference	Input images resized to 180 x 448 pixels. Single-channel images in grey scale

222

223

224

225

226

227

228

229

230

231

232

233

234

Moreover, for the specific case of images representing a single-phase flow (i.e., frames taken for heat flux and wall temperature values below the ONB and therefore, before boiling begins), noise was randomly added to avoid bias during training caused by the similarity between images. In these instances, Gaussian blur and salt-and-pepper noise were randomly introduced into the images [36]. Subsequently, the dataset was partitioned into two parts: 80% for training and 20% for testing [42], [43]. This frequent partitioning ensured that the models were trained on a diverse set of images while also enabling the assessment of their performance on unseen information. Furthermore, training these models involves selecting a proper optimizer, which is a critical component in training neural networks. The optimizer determines how the model weights and parameters are updated during training to increase accuracy while reducing loss. Specifically, the Stochastic Gradient Descent with Momentum (SGDM) optimizer was considered in this work. Its update rule is mathematically expressed according Eq. 1 [44].

$$\begin{aligned} m_i &= \beta m_{i-1} + (1 - \beta) \frac{\delta \mathcal{L}}{\delta w} \\ w_i &= w_{i-1} - \alpha * m_i \end{aligned} \quad \text{Eq.(1)}$$

235

236

237

238

239

240

241

242

243

244

245

246

247

248

249

250

251

252

253

254

Where, m_i represents the momentum at the iteration i , α denotes the learning rate, β is a decay factor of the gradient momentum, and $\frac{\delta \mathcal{L}}{\delta w}$ denotes the rate change of a given cost function \mathcal{L} with respect to the weight [45]. Furthermore, in this study, three metrics were used to evaluate and compare model performance: precision, recall, and F-score. Precision measures the ratio of correctly predicted positive instances to the total predicted positive instances, indicating how accurately the positive predictions reflect overall correctness [46]. Recall quantifies the fraction of actual positive cases that a model successfully identifies as positive. However, precision can be misleading in imbalanced datasets, as a dominant class can inflate precision while neglecting minority classes. Recall focuses only on positive instances and may overlook false positives. The F-score combines precision and recall to provide a balanced assessment. It calculates the harmonic mean of precision and recall, accounting for both false positives and false negatives [47]. Like recall and accuracy, the closer the F-score approaches unity, the better the model performance.

Furthermore, to properly quantify the errors committed by these algorithms, CNN algorithms are also compared with a previous methodology reported in the literature by Hobold and da Silva [20]. This methodology was applied in that previous study to identify pool boiling regimes based on both direct and indirect observations, and here was directly applied to this dataset obtained from the flow boiling setup described in section 2. Specifically, Figure 3 illustrates this approach, which was also implemented using Matlab 2023 and the Statistics and Machine Learning toolbox.

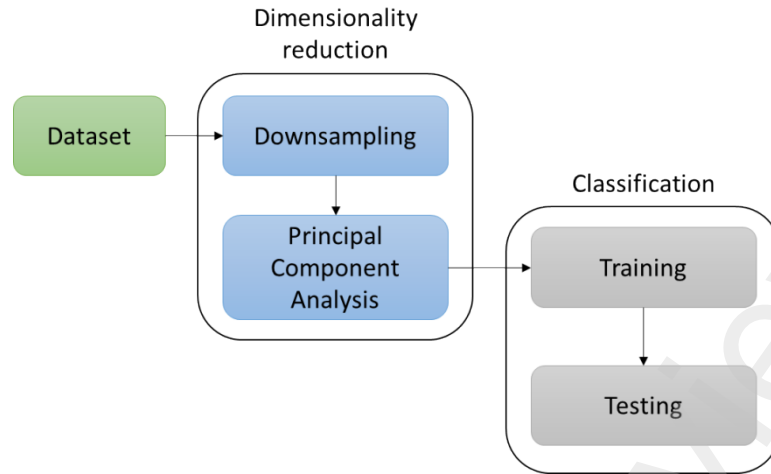


Figure 3. Flowchart of the methodology suggested by Hobold and da Silva [20] for pool boiling images classification by means of both direct and indirect observation.

Specifically, main stages of this approach are as follows:

- **Dimensionality reduction.** To reduce the dimensionality of the images before training machine learning models, Hobold and da Silva [20] proposed a two-stage process. First, downsampling is performed by locally averaging neighbouring pixels, using a downsampling factor of 5 based on image cross-entropy analysis. Second, Principal Component Analysis is applied to further simplify the dataset. PCA reduces the number of variables while retaining most of the variability by obtaining the covariance matrix, from which eigenvalues and eigenvectors are derived [48]. Eigenvectors indicate the directions of maximum variation (principal components), and eigenvalues quantify this variation. The principal components are then ranked by the variance they explain, and a subset is selected to form a reduced dataset that preserves the essential features of the original data, allowing easier analysis with minimal information loss.
- **Classification.** The dataset obtained from the dimensionality reduction stage can be used to train supervised learning algorithms. These groups of algorithms analyse input-output pairs from labelled training data to identify correlations between input and target variables, which can be continuous or categorical. In this study, a Support Vector Machine is employed, similar to the approach taken by Hobold and da Silva [20] in their research. They suggested that the similarity in classification scores across SVM and Neural Networks, both for direct and indirect observation, indicates the suitability of both types of algorithms for pool boiling regime classification. Specifically, SVM classifies both linear and nonlinear data by mapping the feature space to a higher-dimensional space through a nonlinear transformation [49]. The key concept of this algorithm is to find the optimal hyperplane, $f(x)$, as defined mathematically by Eq. 2, which acts as a boundary to separate the data into different classes. This process of identifying the optimal hyperplane involves minimizing a cost function, also specified by Eq. 2 [50].

$$f(x) = \text{sgn} [w \cdot \phi(x') - t]$$

$$\min_{w,b,\xi} \frac{1}{2} \|w\|^2 + C \sum_{i=1}^j \xi \quad \text{Eq.(2)}$$

Where C is a penalty parameter, $\phi(x)$ denotes the mapping function of the input data, t is a bias parameter, w is a weight coefficient vector, ξ denotes a set of slack variables and j is the number of training instances.

4. Results and discussion

This section presents a comparison of the use of DL models for classifying boiling images, alongside a comparison with the dimensionality reduction method proposed by Hobold and da Silva [20]. Specifically, in section 4.1, algorithms are used to classify the boiling regime; section 4.2 focuses on plate type classification; and section 4.3 addresses fluid type classification (note that for this specific section, images without visible bubbles are excluded from the analysis). Finally, section 4.4 reports on four different cases of use of the best performing algorithms.

4.1. Boiling regime classification

The results in Table 2 provide a comparison of Deep Learning algorithms regarding their performance in boiling regime classification. The metrics evaluated include precision, recall, and F-score for three categories: "Non-Boiling", "Boiling", and "Pre-CHF", as described in section 3.

Table 2. Comparison of Deep Learning algorithms and the dimensionality reduction method regarding boiling regime classification.

Metric	Basic CNN		AlexNet		ResNet		InceptionNet		Dimensionality reduction method	
	Train (%)	Test (%)	Train (%)	Test (%)	Train (%)	Test (%)	Train (%)	Test (%)	Train (%)	Test (%)
Precision (Non-Boiling)	100	100	99.39	100	97.85	100	97.14	100	94.00	88.89
Precision (Boiling)	84.97	85.43	98.18	97.95	94.96	93.75	92.13	91.64	81.69	81.30
Precision (Pre-CHF)	89.26	90.25	100	99.28	97.05	98.33	91.75	90.09	88.67	88.12
Recall (Non-Boiling)	23.34	100	100	100	97.25	100	77.93	100	28.66	29.27
Recall (Boiling)	97.24	97.60	99.90	99.81	98.95	99.43	97.55	96.96	97.49	97.16
Recall (Pre-CHF)	81.22	78.92	93.45	92.61	82.88	79.19	82.62	81.25	61.74	59.73
F-score (Non-Boiling)	37.85	100	99.69	100	97.55	100	86.48	100	43.93	44.04
F-score (Boiling)	90.69	91.11	99.03	98.87	96.91	96.50	94.76	94.23	88.89	88.52
F-score (Pre-CHF)	85.05	84.21	96.61	95.83	89.41	87.73	86.94	85.44	72.80	71.20

In terms of precision metrics, all CNN models demonstrate strong performance across both training and testing datasets. For example, Basic CNN achieved 89.26% precision in training and 90.25% in testing for the "Pre-CHF" instance, indicating minimal overfitting. During testing, AlexNet, ResNet, InceptionNet, and Basic CNN all achieved 100% precision in identifying instances without boiling. AlexNet and ResNet achieved high precision rates of 97.95% and 93.75%, respectively, in the "Boiling" category, while InceptionNet closely followed with 91.64%. In contrast, Basic CNN showed lower precision in both the "Boiling" (85.43%) and "Pre-CHF" (89.26%) categories, where AlexNet and ResNet achieved values greater than 95%, indicating their superior performance compared to Basic CNN.

Regarding recall, AlexNet achieved high scores across all categories (above 92%), outperforming InceptionNet and ResNet, which achieved lesser metrics with minimum values around 80%. The Basic CNN exhibited notably lower recall rates, particularly in the "Non-Boiling" category (less than 30%). This difference between precision and recall suggests that while the Basic CNN accurately identifies instances labelled as "Non-Boiling" (high precision), it may miss actual instances (low recall), possibly due to conservative predictions.

Comparatively, the dimensionality reduction method showed performance similar to the Basic CNN but fell behind advanced CNN models such as AlexNet, ResNet, and InceptionNet in terms of F-scores. In fact, this methodology achieved 44.04% and 71.20% for "Non-Boiling" and "Pre-CHF", respectively, in F-scores, which were lower than the scores above 85% achieved by

advanced CNNs. It is also important to note that the F-score values reported by Hobold and da Silva [20] in their study ranged from 66% to 95%, depending on the specific category being classified. The discrepancies observed in these ranges can be attributed to the use of different types of images (e.g., flow boiling in this study versus pool boiling in that previous work) and varying experimental conditions.

Overall, these results suggest that advanced CNN models involve superior capabilities over both Basic CNN and the dimensionality reduction method in accurately classifying boiling regimes within this specific dataset. Notably, AlexNet achieved the highest F-scores in the testing dataset (e.g., 95.8% for the "Pre-CHF" class), highlighting its effectiveness in this classification task.

4.2. Heating Plate-type classification

Table 3 provides a comparative analysis of the results of these algorithms in classifying plate types, which reflects some trends also observed for the classification of boiling regimes (section 4.1). In this sense, ResNet and InceptionNet achieved precision rates above 95% across categories such as "Non-Boiling" and "Boiling" in the boiling regime, demonstrating their accuracy in identifying these instances. Likewise, in the plate type dataset, these models maintained precision rates above 95% in both "Non-Textured" and "Micro-Textured" categories, underscoring their effectiveness in precise classification tasks.

Table 3. Comparison of Deep Learning algorithms and the dimensionality reduction method regarding plate-type classification.

Metric	Basic CNN		AlexNet		ResNet		InceptionNet		Dimensionality reduction method	
	Train (%)	Test (%)	Train (%)	Test (%)	Train (%)	Test (%)	Train (%)	Test (%)	Train (%)	Test (%)
Precision (Non-Textured)	59.48	59.64	75.57	75.97	97.32	97.01	98.19	97.83	83.25	81.27
Precision (Micro-Textured)	100	100	100	100	95.44	93.68	97.58	98.52	86.40	81.76
Recall (Non-Textured)	100	100	100	100	96.87	95.58	98.53	99.01	92.19	89.34
Recall (Micro-Textured)	0.12	0.71	52.56	53.76	96.09	95.69	97.33	96.40	72.78	69.89
F-score (Non-Textured)	74.59	74.72	86.08	86.34	97.10	96.29	98.36	98.29	87.49	85.11
F-score (Micro-Textured)	0.25	1.428	68.90	69.93	95.76	94.68	97.58	97.45	79.01	75.36

However, there are notable differences in recall metrics between the boiling regime and plate type classification. In the boiling regime, AlexNet achieved recall rates above 90% across all categories. However, the plate type dataset exhibited more variability in terms of this metric. For instance, in the "Micro-Textured" category, AlexNet achieved recall rates of 52% during training and 53% during testing. In contrast, ResNet and InceptionNet demonstrated superior recall performance, with ResNet exceeding a value of 95% for both classes in the plate type dataset, indicating a more reliable model choice compared to AlexNet for this specific application. Furthermore, it is also important to note the significant disparity between recall and precision metrics observed with AlexNet. For example, in the "Micro-Textured" category during testing, AlexNet achieved a precision of 100% but a recall of only 53.76%. This discrepancy underscores the trade-off between precision and recall metrics: high precision reflects the ability to minimize false positives, while low recall indicates its challenge in correctly identifying positive instances, leading to more false negatives.

Regarding the dimensionality reduction method proposed by Hobold and da Silva [20], it demonstrated improved precision and recall for non-textured images compared to Basic CNN, achieving a test precision of 81.27% and a recall of 89.34%. However, it was clearly outperformed by ResNet (97.01% precision, 95.58% recall) and InceptionNet (97.83% precision, 99.01%

recall). For micro-textured data, the dimensionality reduction method showed the lowest precision (81.76%) among all methods, while Basic CNN and AlexNet achieved perfect scores of 100%, and ResNet and InceptionNet achieved 93.68% and 98.52%, respectively. Despite this, the dimensionality reduction method exhibited better recall (69.89%) compared to Basic CNN (lesser than 10%). Therefore, these results suggests that, while the methodology reported by Hobold and da Silva [20] demonstrated improvements over a basic CNN, it showed lesser effectiveness compared to advanced models like ResNet and InceptionNet across all metrics.

4.3. Fluid-type classification

Regarding the application of the algorithms for fluid-type classification based on the presence of bubbles in the images, Table 4 presents the results obtained by means of precision, recall and F-score metrics.

Table 4. Comparison of Deep Learning algorithms and the Dimensionality reduction method regarding fluid-type classification.

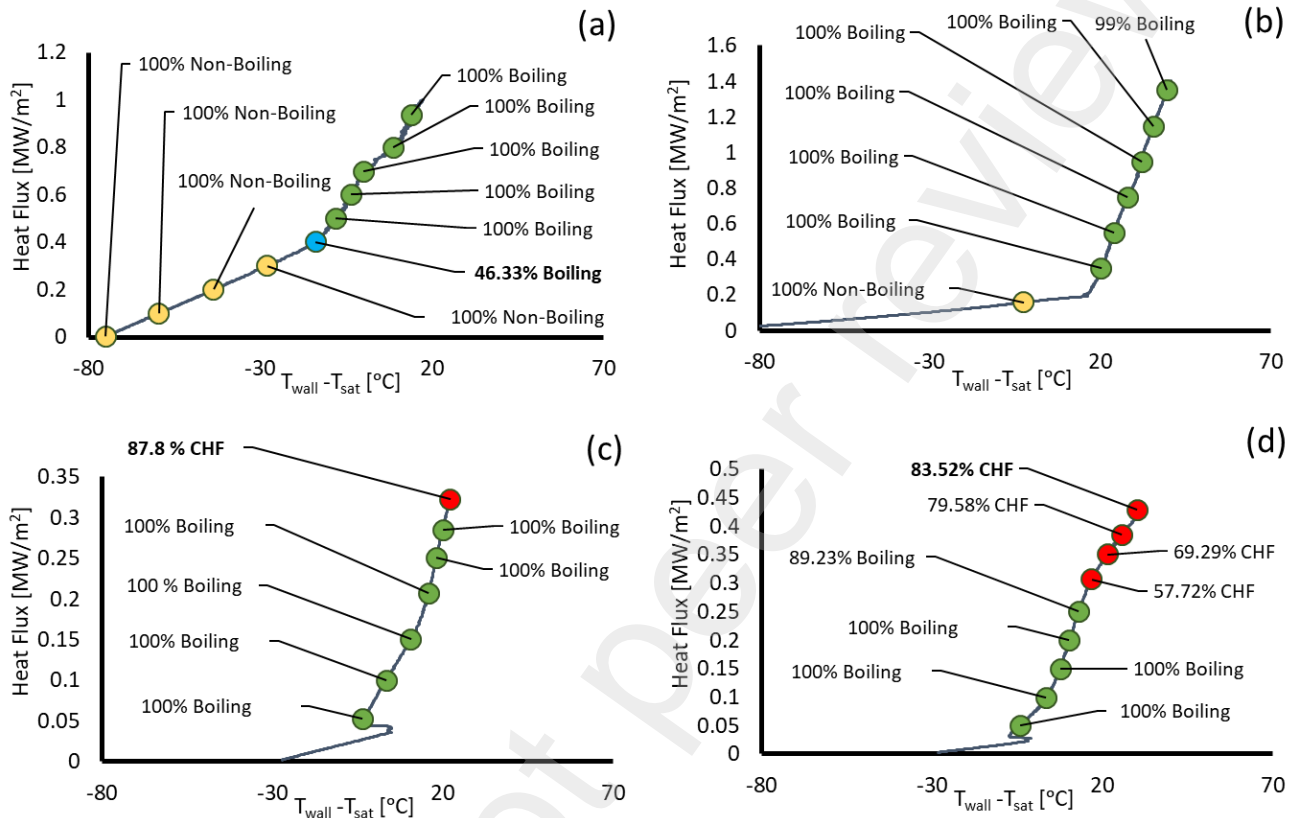
Metric	Basic CNN		AlexNet		ResNet		InceptionNet		Dimensionality reduction method	
	Train (%)	Test (%)	Train (%)	Test (%)	Train (%)	Test (%)	Train (%)	Test (%)	Train (%)	Test (%)
Precision (Water)	81.10	75.48	100	100	97.74	98.17	98.64	99.39	76.47	75.00
Precision (Hydrofluoroether)	60.93	100	96.96	100	98.99	100	96.83	100	80.99	77.95
Precision (EG-Water)	69.42	71.28	97.69	96.53	96.86	92.93	96.25	93.88	73.80	74.24
Recall (Water)	71.12	71.34	100	100	98.93	98.17	99.54	100	63.22	64.02
Recall (Hydrofluoroether)	51.07	100	99.61	100	0.9571	100	95.32	100	83.04	77.34
Recall (EG-Water)	85.85	83.23	99.70	100	0.9812	98.84	96.53	97.68	84.56	84.97
F-score (Water)	75.78	73.35	100	100	99.61	98.17	99.09	99.69	69.21	69.07
F-score (Hydrofluoroether)	55.56	100	98.26	100	97.32	100	96.07	100	82.00	77.65
F-score (EG-Water)	76.77	76.80	98.68	98.23	97.49	95.79	96.39	95.75	78.82	79.25

In this sense, AlexNet was found as the best-performing method for this specific dataset, achieving near-perfect precision, recall, and F-score across all fluid types, with its lowest score being 96.53% precision for testing EG-Water. ResNet performs comparably, particularly with Water and Hydrofluoroether. However, for EG-Water, its performance is slightly lower, with 96.86% precision and 98.84% recall in testing. InceptionNet also demonstrates high performance, especially in recall and F-score for Water and Hydrofluoroether, although it also shows a minor decline in precision for EG-Water (93.88%).

The Basic CNN, on the other hand, shows significantly lower performance metrics across all fluid types compared to the advanced models. Its precision, recall, and F-score for Water, Hydrofluoroether, and EG-Water are markedly lower, particularly in the testing set where scores hover around the 70-75% range. This indicates that the Basic CNN is not as effective as the more advanced architectures like AlexNet, ResNet, and InceptionNet.

Similarly, the Dimensionality Reduction Method performs worse compared to AlexNet, ResNet, and InceptionNet. While it shows improved performance over the Basic CNN, especially in recall and F-score for Hydrofluoroether and EG-Water, it still falls short with relatively lower scores. For example, it has a precision of 75% for Water and about 77-79% for Hydrofluoroether and EG-Water in testing, clearly below the performance of the CNN models. Furthermore, it should be also noted that for this specific application, F-scores of the dimensionality reduction method are also in the range reported by Hobold and da Silva [20] for boiling classification purposes (ranging between 56% - 97%).

394 To evaluate the use of these deep learning models, four cases of use were considered, two
 395 of which reached critical heat flux conditions. Figure 4 displays the boiling curve obtained for
 396 each case in four separate panels, showing the relationship between heat flux and the excess
 397 temperature, $\Delta T = T_{wall} - T_{saturation}$. The circular markers represent recording points, with
 398 labels showing results averaged over 1876 frames, used to classify the boiling regime according
 399 to the AlexNet network.



401 **Figure 4.** Boiling curves: (a) Water on a non-textured plate with an inlet temperature of 40°C, an
 402 inlet velocity of 0.8 m/s, and a pressure of 1.75 bar. (b) EG - Water, non-textured plate, 20°C, 0.2 m/s, 1.75
 403 bar. (c) Hydrofluoroether on a non-textured plate with an inlet temperature of 40°C, an inlet velocity of 0.4
 404 m/s, and a pressure of 1.3 bar. (d) Hydrofluoroether, textured plate, 40°C, 0.2 m/s, 1.3 bar.

405 In all these curves, the initial straight line corresponds to a single-phase stage. A change in
 406 the slope marks the ONB and the beginning of the nucleate boiling regime. As shown in Figure
 407 4.a, the yellow markers, representing points in this initial single-phase zone, accurately classify
 408 the "Non-Boiling" regime. Then, the blue marker, located at the ONB where bubbles start to form,
 409 shows that 46.33% of frames at this point are classified as involving nucleate boiling, consistent
 410 with the onset of this phase. Beyond this point, all remaining images are correctly classified within
 411 the nucleate boiling regime (green markers).

412 A similar trend is observed for the EG-Water case in Figure 4.b: The first yellow marker
 413 on the initial straight line aligns with the single-phase region. Once the slope changes, indicating
 414 the transition to nucleate boiling, all subsequent recording points (green markers) are accurately
 415 classified within this boiling regime.

416 For the Hydrofluoroether tests shown in Figure 4.c and 4.d, where CHF conditions were
 417 reached, the red-circled markers highlight video records where over 50% of the frames were
 418 classified as pre-CHF. All these frames were classified as pre-CHF after the onset of nucleate
 419 boiling. Specifically, Figure 4.d demonstrates that the proportion of images classified as pre-CHF
 420 increases with rising heat flux within the red-circled markers. At the final recording point, about

85% of the frames are classified as pre-CHF, signalling a potentially dangerous situation for the experimental setup.

Finally, regarding fluid and plate type classifications, the case shown in Figure 4.d yielded the lowest performance metric. Specifically, 92.9% of frames in the nucleate boiling zone were accurately classified as Hydrofluoroether, and 95.6% were correctly identified as involving a textured plate. These results align with the metrics obtained during training and testing according to sections 4.2 and 4.3.

5. Conclusions

This study focuses on classifying images captured from a flow boiling setup based on three main characteristics: the boiling condition (No-Boiling, Nucleate Boiling, or Pre-CHF state), plate type (non-textured or micro-textured), and fluid type (EG-Water, Hydrofluoroether, or Water). The analysis compares three CNN algorithms (ResNet, AlexNet, and InceptionNet) with a basic CNN used as a reference. Additionally, these deep learning models are compared with a previously described approach [20], referred to in this work as the "Dimensionality reduction method". Specifically, this method involves a downsampling process followed by a Machine Learning stage using an SVM algorithm.

Regarding the boiling condition, AlexNet demonstrated superior performance with an F-score exceeding 95%, while ResNet and InceptionNet showed comparable results. All three algorithms significantly outperformed both the basic CNN and the Dimensionality reduction method, which achieved F-scores below 50%.

In the classification of plate type, InceptionNet and ResNet exhibited better performance compared to AlexNet. Although the Dimensionality reduction method showed improvements over the basic CNN, it was less effective than advanced models like ResNet and InceptionNet across all metrics. Lastly, in fluid type classification, the Dimensionality reduction method again underperformed compared to AlexNet, ResNet, and InceptionNet. For instance, it achieved a precision of 75% for Water and approximately 77-79% for Hydrofluoroether and EG-Water during testing, which was notably lower than the CNN models achieving around 90%.

Finally, four use cases (boiling curves) were analyzed, with the performance of the algorithms for these cases aligning with the metrics obtained during testing and training.

These results highlight the importance of selecting an appropriate classification algorithm, as the performance of algorithms can vary significantly based on the specific task. Furthermore, CNN models widely used in other scientific domains, such as AlexNet, ResNet, and InceptionNet, have demonstrated their value in effectively classifying images related to boiling phenomena.

Acknowledgments

Authors are grateful to the Spanish Ministry for Science and Innovation for the financial support through the PID2020-114742RB-I00 project. Funding for open access charge: Universidade de Vigo/CISUG.

Appendix A

This section includes representative images from the dataset used in this study. Specifically, Figure A.1 shows an example of three frames, where each of them was labelled with one of the boiling states (Non-Boiling, Nucleate Boiling and Pre-CHF).

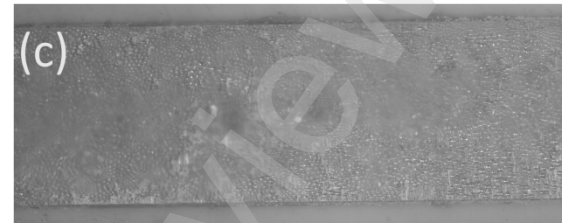
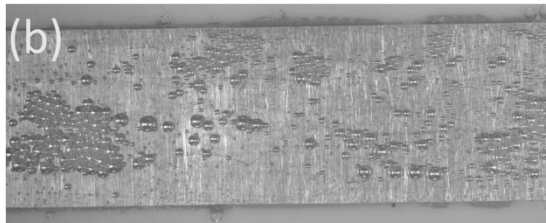
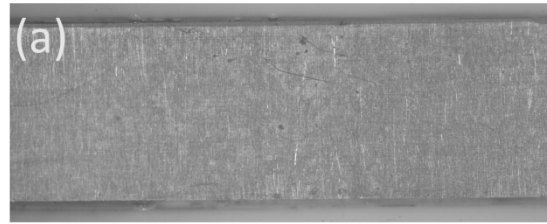


Figure A. 1 Examples of images considered in this study labelled as **(a)** No-Boiling. **(b)** Nucleate Boiling. **(c)** Pre-CHF state.

In Figure A.2, two images of the two different heating plate types can be found (non-textured or micro-textured).

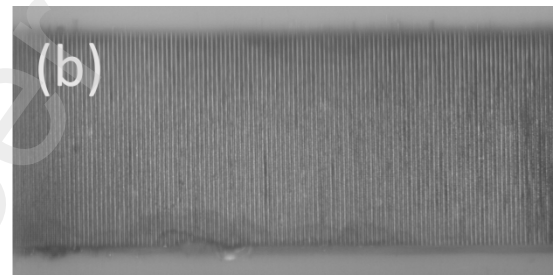
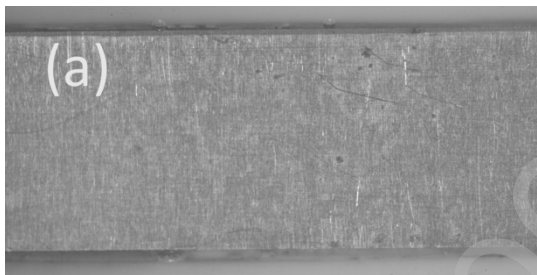


Figure A. 2 Examples of images considered in this study labelled as **(a)** Non-textured. **(b)** Micro-textured.

In Figure A.3, bubbles corresponding to the three fluids considered in this work (EG-Water, Hydrofluoroether and Water) can be found.

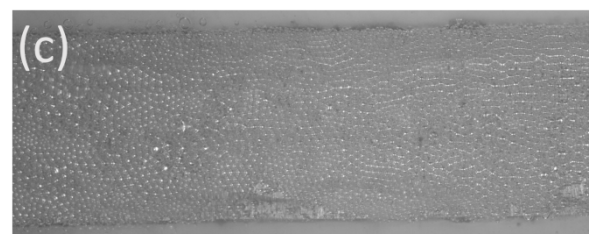
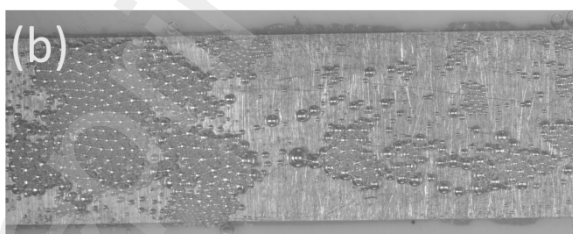
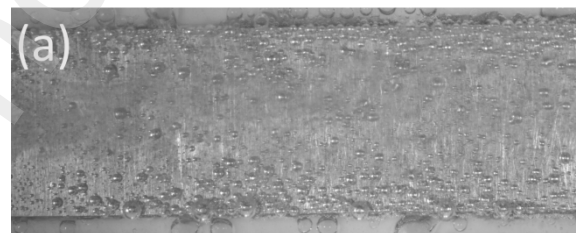


Figure A. 3 Examples of images considered in this study labelled as **(a)** Water. **(b)** EG-Water. **(c)** Hydrofluoroether.

Appendix B

In Table B. 1, the pooling and convolutional operations composing the Basic CNN, inspired by the sample structure found in references [37] and [38], can be found.

Table B. 1 Details of each layer composing the basic CNN used in this work.

<i>Sequence of layers</i>	<i>Details</i>
Convolution (1)	Kernel size = [3 * 3], Kernel number = [16], Stride = [1], ReLu
Pooling (2)	Pooling type = Max Pooling, Kernel size = [2 * 2], Stride = [2]
Convolution (3)	Kernel size = [3 * 3], Kernel number = [16], Stride = [1], ReLu
Pooling (4)	Pooling type = Max Pooling, Kernel size = [2 * 2], Stride = [2]
Fully Connected (5)	Softmax

Table B. 2 includes the parameters of each layer for the AlexNet structure [36], [37].

Table B. 2 AlexNet model.

<i>Sequence of layers</i>	<i>Details</i>
Convolution (1)	Kernel size = [11 * 11], Kernel number = [96], Stride = [4], ReLu
Pooling (2)	Pooling type = Max Pooling, Kernel size = [3 * 3]
Convolution (3)	Kernel size = [5 * 5], Kernel number = [256], Stride = [1], ReLu
Pooling (4)	Pooling type = Max Pooling, Kernel size = [3 * 3]
Convolution (5)	Kernel size = [3 * 3], Kernel number = [384], Stride = [1], ReLu
Convolution (6)	Kernel size = [3 * 3], Kernel number = [384], Stride = [1], ReLu
Convolution (7)	Kernel size = [3 * 3], Kernel number = [256], Stride = [1], ReLu
Pooling (8)	Pooling type = Max Pooling, Kernel size = [3 * 3]
Fully Connected (9)	4096 neurons
Fully Connected (10)	4096 neurons
Fully Connected (11)	Softmax

Table B. 3 presents the parameters of each stage for the ResNet structure [41], [45].

Table B. 3 ResNet model.

<i>ResNet Stages</i>	<i>Details</i>
Convolutional Stage 1	(Kernel size = [7 * 7], Kernel number = [64]) + Max Pooling [3 * 3]
Convolutional Stage 2	Kernel size = [3 * 3], Kernel number = [64]
Convolutional Stage 3	Kernel size = [3 * 3], Kernel number = [128]
Convolutional Stage 4	Kernel size = [3 * 3], Kernel number = [256]
Convolutional Stage 5	Kernel size = [3 * 3], Kernel number = [512]
Pooling	Pooling type = Average Pooling, Kernel size = [7 * 7]
Final stage	Softmax

References

- [1] M. Jamialahmadi, C. Branch, and H. Müller-Steinhagen, "Augmentation of Nucleate Boiling by Additives," in *Transport Phenomena in Heat and Mass Transfer*, J. A. REIZES, Ed. Amsterdam: Elsevier, 1992, pp. 539–549. Doi: 10.1016/B978-0-444-89851-7.50052-2.
- [2] Z. Cao, Z. Wu, M. Faghri, and B. Sundén, "Coating engineering for boiling heat transfer toward immersion cooling," in *Advances in Heat Transfer*, vol. 53, J. P. Abraham, J. M. Gorman, and W. Minkowycz, Eds. Elsevier, 2021, pp. 97–158. Doi: 10.1016/bs.aiht.2021.06.002.
- [3] Y. Soffer, Y. Aharon, and G. Ziskind, "Experimental investigation on incipient boiling in narrow closed gaps with water," *International Journal of Thermal Sciences*, vol. 191, p. 108333, 2023. Doi: 10.1016/j.ijthermalsci.2023.108333.
- [4] S. Ni, C. Pan, T. Hibiki, and J. Zhao, "Applications of nucleate boiling in renewable energy and thermal management and recent advances in modeling—a review," *Energy*, vol. 289, p. 129962, 2024. Doi: 10.1016/j.energy.2023.129962.

- [5] R. I. Elghanam, M. M. E. Fawal, R. A. Aziz, M. H. Skr, and A. H. Khalifa, "Experimental study of nucleate boiling heat transfer enhancement by using surfactant," *Ain Shams Engineering Journal*, vol. 2, no. 3, pp. 195–209, 2011. Doi: 10.1016/j.asej.2011.09.001.
- [6] G. Liang and I. Mudawar, "Pool boiling critical heat flux (CHF) – Part 1: Review of mechanisms, models, and correlations," *International Journal of Heat and Mass Transfer*, vol. 117, pp. 1352–1367, 2018. Doi: 10.1016/j.ijheatmasstransfer.2017.09.134.
- [7] A. Cabarcos, C. Paz, E. Suarez, and J. Vence, "Application of supervised learning algorithms for temperature prediction in nucleate flow boiling," *Applied Thermal Engineering*, vol. 240, p. 122155, 2024. Doi: 10.1016/j.applthermaleng.2023.122155.
- [8] D. H. Kam, Y. H. Jeong, and H. C. NO, "A heat transfer model development for CHF prediction with consideration of dry patch characteristics," *International Journal of Heat and Mass Transfer*, vol. 148, p. 118812, 2020. Doi: 10.1016/j.ijheatmasstransfer.2019.118812.
- [9] R. Hernandez, C. P. Folsom, N. E. Woolstenhulme, C. B. Jensen, J. D. Bess, J. P. Gorton, and N. R. Brown, "Review of pool boiling critical heat flux (CHF) and heater rod design for CHF experiments in TREAT," *Progress in Nuclear Energy*, vol. 123, p. 103303, 2020. Doi: 10.1016/j.pnucene.2020.103303.
- [10] A. K. Dixit, R. Kumar, and A. K. Das, "Investigation of film boiling at a liquid-liquid contact," *International Journal of Heat and Mass Transfer*, vol. 196, p. 123234, 2022. Doi: 10.1016/j.ijheatmasstransfer.2022.123234.
- [11] P. Goel, A. K. Nayak, P. P. Kulkarni, and J. B. Joshi, "Experimental study on bubble departure characteristics in subcooled nucleate pool boiling," *International Journal of Multiphase Flow*, vol. 89, pp. 163–176, 2017. Doi: 10.1016/j.ijmultiphaseflow.2016.10.012.
- [12] L. Yuan, F. Hong, and P. Cheng, "Pool boiling enhancement through a guidance structure mounted above heating surface," *International Journal of Heat and Mass Transfer*, vol. 139, pp. 751–763, 2019. Doi: 10.1016/j.ijheatmasstransfer.2019.05.067.
- [13] V. I. Sharma, J. Buongiorno, T. J. McKrell, and L. W. Hu, "Experimental investigation of transient critical heat flux of water-based zinc-oxide nanofluids," *International Journal of Heat and Mass Transfer*, vol. 61, pp. 425–431, 2013. Doi: 10.1016/j.ijheatmasstransfer.2013.02.009.
- [14] K. Sinha, D. Ranjan, N. Kumar, M. Q. Raza, and R. Raj, "Simultaneous audio-visual-thermal characterization of transition boiling regime," *Experimental Thermal and Fluid Science*, vol. 118, p. 110162, 2020. Doi: 10.1016/j.expthermflusci.2020.110162.
- [15] D. D. Hall and I. Mudawar, "Critical heat flux (CHF) for water flow in tubes—I. Compilation and assessment of world CHF data," *International Journal of Heat and Mass Transfer*, vol. 43, no. 14, pp. 2573–2604, 2000. Doi: 10.1016/S0017-9310(99)00191-X.
- [16] A. Z. Mesquita and R. R. Rodrigues, "Detection of the Departure from Nucleate Boiling in Nuclear Fuel Rod Simulators," *International Journal of Nuclear Energy*, vol. 2013, 2013.
- [17] A. B. Ponter and C. P. Haigh, "Sound emission and heat transfer in low pressure pool boiling," *International Journal of Heat and Mass Transfer*, vol. 12, no. 4, pp. 413–428, 1969. Doi: 10.1016/0017-9310(69)90137-9.
- [18] K. Sinha, D. Ranjan, M. Q. Raza, N. Kumar, S. Kaner, A. Thakur, and R. Raj, "In-situ acoustic detection of critical heat flux for controlling thermal runaway in boiling systems," *International Journal of Heat and Mass Transfer*, vol. 138, pp. 135–143, 2019. Doi: 10.1016/j.ijheatmasstransfer.2019.04.029.
- [19] Y. Ueki and K. Ara, "Proof of concept of acoustic detection of boiling inception and state transition using deep neural network," *International Communications in Heat and Mass Transfer*, vol. 129, p. 105675, 2021. Doi: 10.1016/j.icheatmasstransfer.2021.105675.
- [20] G. M. Hobold and A. K. da Silva, "Machine learning classification of boiling regimes with low speed, direct and indirect visualization," *International Journal of Heat and Mass Transfer*, vol. 125, pp. 1296–1309, 2018. Doi: 10.1016/j.ijheatmasstransfer.2018.04.156.
- [21] F. Al-Hindawi, T. Soori, H. Hu, M. M. R. Siddiquee, H. Yoon, T. Wu, and Y. Sun, "A framework for generalizing critical heat flux detection models using unsupervised image-to-image translation," *Expert Systems with Applications*, vol. 227, p. 120265, 2023. Doi: 10.1016/j.eswa.2023.120265.
- [22] G. M. Hobold and A. K. da Silva, "Visualization-based nucleate boiling heat flux quantification using machine learning," *International Journal of Heat and Mass Transfer*, vol. 134, pp. 511–520, 2019. Doi: 10.1016/j.ijheatmasstransfer.2018.12.170.
- [23] R. Yamashita, M. Nishio, R. K. G. Do, and K. Togashi, "Convolutional neural networks: an overview and application in radiology," *Insights into Imaging*, vol. 9, pp. 611–629, 2018.
- [24] J. Soibam, V. Scheiff, I. Aslanidou, K. Kyprianidis, and R. B. Fdhila, "Application of deep learning for segmentation of bubble dynamics in subcooled boiling," *International Journal of Multiphase Flow*, vol. 169, p. 104589, 2023. Doi: 10.1016/j.ijmultiphaseflow.2023.104589.

- [25] Y. Suh, R. Bostanabad, and Y. Won, "Deep learning predicts boiling heat transfer," *Sci Rep*, vol. 11, 2021.
- [26] F. Nie, H. Wang, Q. Song, Y. Zhao, J. Shen, and M. Gong, "Image identification for two-phase flow patterns based on CNN algorithms," *International Journal of Multiphase Flow*, vol. 152, p. 104067, 2022. Doi: 10.1016/j.ijmultiphaseflow.2022.104067.
- [27] M. M. Rashidi, M. A. Nazari, C. Harley, E. Momoniat, I. Mahariq, and N. Ali, "Applications of machine learning methods for boiling modeling and prediction: A comprehensive review," *Chemical Thermodynamics and Thermal Analysis*, vol. 8, p. 100081, 2022. Doi: 10.1016/j.ctta.2022.100081.
- [28] S. M. Rassoulinejad-Mousavi, F. Al-Hindawi, T. Soori, A. Rokoni, H. Yoon, H. Hu, T. Wu, and Y. Sun, "Deep learning strategies for critical heat flux detection in pool boiling," *Applied Thermal Engineering*, vol. 190, p. 116849, 2021. Doi: 10.1016/j.applthermaleng.2021.116849.
- [29] I. H. Sarker, "Machine Learning: Algorithms, Real-World Applications and Research Directions," *SN Computer Science*, vol. 2, 2021.
- [30] M. Conde-Fontenla, C. Paz, M. Concheiro, and G. Ribatski, "On the width and mean value of bubble size distributions under subcooled flow boiling," *Experimental Thermal and Fluid Science*, vol. 124, p. 110368, 2021. Doi: 10.1016/j.expthermflusci.2021.110368.
- [31] C. Paz, M. Conde, J. Porteiro, and M. Concheiro, "Effect of heating surface morphology on the size of bubbles during the subcooled flow boiling of water at low pressure," *International Journal of Heat and Mass Transfer*, vol. 89, pp. 770–782, 2015. Doi: 10.1016/j.ijheatmasstransfer.2015.06.003.
- [32] H. Jo, H. S. Ahn, S. Kang, and M. H. Kim, "A study of nucleate boiling heat transfer on hydrophilic, hydrophobic and heterogeneous wetting surfaces," *International Journal of Heat and Mass Transfer*, vol. 54, no. 25, pp. 5643–5652, 2011. Doi: 10.1016/j.ijheatmasstransfer.2011.06.001.
- [33] Y. Chen, R. Kong, and L. Kong, "Applications of artificial intelligence in astronomical big data," in *Big Data in Astronomy*, L. Kong, T. Huang, Y. Zhu, and S. Yu, Eds. Elsevier, 2020, pp. 347–375. Doi: 10.1016/B978-0-12-819084-5.00006-7.
- [34] M. Valizadeh and S. J. Wolff, "Convolutional Neural Network applications in additive manufacturing: A review," *Advances in Industrial and Manufacturing Engineering*, vol. 4, p. 100072, 2022. Doi: 10.1016/j.aime.2022.100072.
- [35] S. Indolia, A. K. Goswami, S. P. Mishra, and P. Asopa, "Conceptual Understanding of Convolutional Neural Network- A Deep Learning Approach," *Procedia Computer Science*, vol. 132, pp. 679–688, 2018. Doi: 10.1016/j.procs.2018.05.069.
- [36] D. Raval and J. N. Undavia, "A Comprehensive assessment of Convolutional Neural Networks for skin and oral cancer detection using medical images," *Healthcare Analytics*, vol. 3, p. 100199, 2023. Doi: 10.1016/j.health.2023.100199.
- [37] S. Kiranyaz, O. Avci, O. Abdeljaber, T. Ince, M. Gabbouj, and D. J. Inman, "1D convolutional neural networks and applications: A survey," *Mechanical Systems and Signal Processing*, vol. 151, p. 107398, 2021. Doi: 10.1016/j.ymssp.2020.107398.
- [38] S. Zahia, M. B. G. Zapirain, X. Sevillano, A. González, P. J. Kim, and A. Elmaghraby, "Pressure injury image analysis with machine learning techniques: A systematic review on previous and possible future methods," *Artificial Intelligence in Medicine*, vol. 102, p. 101742, 2020. Doi: 10.1016/j.artmed.2019.101742.
- [39] Y. Chandola, J. Virmani, H. S. Bhadauria, and P. Kumar, "End-to-end pre-trained CNN-based computer-aided classification system design for chest radiographs," in *Deep Learning for Chest Radiographs*, Y. Chandola, J. Virmani, H. S. Bhadauria, and P. Kumar, Eds. Academic Press, 2021, pp. 117–140. Doi: 10.1016/B978-0-323-90184-0.00011-4.
- [40] H. Ran, S. Wen, K. Shi, and T. Huang, "Stable and compact design of Memristive GoogLeNet Neural Network," *Neurocomputing*, vol. 441, pp. 52–63, 2021. Doi: 10.1016/j.neucom.2021.01.122.
- [41] E. Kim, G. S. Dahiya, S. Løset, and R. Skjetne, "Can a computer see what an ice expert sees? Multilabel ice objects classification with convolutional neural networks," *Results in Engineering*, vol. 4, p. 100036, 2019. Doi: 10.1016/j.rineng.2019.100036.
- [42] K. Liu, Z. Dai, R. Zhang, J. Zheng, J. Zhu, and X. Yang, "Prediction of the sulfate resistance for recycled aggregate concrete based on ensemble learning algorithms," *Construction and Building Materials*, vol. 317, p. 125917, 2022. Doi: 10.1016/j.conbuildmat.2021.125917.
- [43] B. Erkeyman, E. Erdem, T. Aydin, and Z. Mahmat, "New Artificial intelligence approaches for brand switching decisions," *Alexandria Engineering Journal*, vol. 63, pp. 625–643, 2023. Doi: 10.1016/j.aej.2022.11.043.
- [44] E. Okafor, M. Oyediji, and M. Alfarraj, "Deep reinforcement learning with light-weight vision model for sequential robotic object sorting," *Journal of King Saud University - Computer and Information Sciences*, vol. 36, no. 1, p. 101896, 2024. Doi: 10.1016/j.jksuci.2023.101896.

- [45] D. Sarwinda, R. H. Paradisa, A. Bustamam, and P. Anggia, "Deep Learning in Image Classification using Residual Network (ResNet) Variants for Detection of Colorectal Cancer," *Procedia Computer Science*, vol. 179, pp. 423–431, 2021. Doi: 10.1016/j.procs.2021.01.025.
- [46] M. A. Islam and G. Olm, "Deep learning techniques to detect rail indications from ultrasonic data for automated rail monitoring and maintenance," *Ultrasonics*, vol. 140, p. 107314, 2024. Doi: 10.1016/j.ultras.2024.107314.
- [47] H. Belyadi and A. Haghighat, "Supervised learning," in *Machine Learning Guide for Oil and Gas Using Python*, H. Belyadi and A. Haghighat, Eds. Gulf Professional Publishing, 2021, pp. 169–295. Doi: 10.1016/B978-0-12-821929-4.00004-4.
- [48] F. Guillon, N. Gierlinger, M.-F. Devaux, and A. Gorzsás, "In situ imaging of lignin and related compounds by Raman, Fourier-transform infrared (FTIR) and fluorescence microscopy," in *Lignin and Hydroxycinnamic Acids: Biosynthesis and the Buildup of the Cell Wall*, vol. 104, R. Sibout, Ed. Academic Press, 2022, pp. 215–270. Doi: 10.1016/bs.abr.2022.03.009.
- [49] J. Cai, "Applying support vector machine to predict the critical heat flux in concentric-tube open thermosiphon," *Annals of Nuclear Energy*, vol. 43, pp. 114–122, 2012. Doi: 10.1016/j.anucene.2011.12.029.
- [50] A. Urso, A. Fiannaca, M. L. Rosa, V. Ravì, and R. Rizzo, "Data Mining: Classification and Prediction," in *Encyclopedia of Bioinformatics and Computational Biology*, S. Ranganathan, M. Gribskov, K. Nakai, and C. Schönbach, Eds. Oxford: Academic Press, 2019, pp. 384–402. Doi: 10.1016/B978-0-12-809633-8.20461-5.